REGULAR PAPER

Numerical simulations for ferromagnetic resonance of nano-size island structures probed by radio-frequency scanning tunneling microscopy

To cite this article: Yudai Sato *et al* 2022 *Jpn. J. Appl. Phys.* **61** 025001

Japanese Journal of Applied Physics **61**, 025001 (2022) **REGULAR PAPER**
https://doi.org/**10.35848/1347-4065/ac4556**

Numerical simulations for ferromagnetic resonance of nano-size island structures probed by radio-frequency scanning tunneling microscopy

Yudai Sato[1], Masahiro Haze[1], Hung-Hsiang Yang[1,2], Kanta Asakawa[1,3], Susumu Takahashi[1,4,5], and Yukio Hasegawa[1*]

[1]*Institute for Solid State Physics, the University of Tokyo, 5-1-5, Kashiwa-no-ha, Kashiwa, Chiba 277-8581, Japan*
[2]*Physical Institute, Karlsruhe Institute of Technology, Karlsruhe 76131, Germany*
[3]*Department of Applied Physics, Tokyo University of Agriculture and Technology, 2-24-16, Nakacho, Koganei, Tokyo 184-8588, Japan*
[4]*Department of Chemistry, University of Southern California, Los Angeles CA 90089, United States of America*
[5]*Department of Physics & Astronomy, University of Southern California, Los Angeles CA 90089, United States of America*

[*]E-mail: hasegawa@issp.u-tokyo.ac.jp

Received October 17, 2021; revised December 19, 2021; accepted December 20, 2021; published online January 31, 2022

We numerically calculated ferromagnetic resonance (FMR) spectra taken on a single-domain nano-size ferromagnetic island structure in the configuration of radio-frequency (RF) scanning tunneling microscopy, where RF electromagnetic waves are introduced into the tunneling gap through the probe tip. In this scheme, near-field in-plane azimuthal RF magnetic field induces FMR of an out-of-plane magnetized island situated below the tip under the external out-of-plane magnetic field. The amount of the magnetization of the island is effectively reduced by the resonance and the reduction can be detected from the spin-polarized tunneling conductance. From the calculated spectra we found that the FMR signal becomes larger with a smaller tip-sample distance and a sharper tip. It is also revealed that the azimuthal RF magnetic field exerted on the island and therefore the FMR signal are enhanced when a tip is located near the edge of the island.

1. Introduction

Nano-sized magnetic materials have been studied extensively for fundamental sciences of magnetism and future applications of magnetic storage devices such as highly integrated magnetic random access memories and largely dense hard disk drives. The control and detection of dynamics in individual magnetic materials are key ingredients for designing and fabricating desired magnetic materials.[1–3] Ferromagnetic resonance (FMR) spectroscopy, which enables the detection of collective magnetic excitations, is a powerful technique to investigate magnetic materials. FMR allows measuring the magnetization, local dynamical fields, and relaxation times of magnetic materials. FMR can generate spin currents by spin pumping in ferromagnetic/paramagnetic hybrid systems.[4–6] FMR has also been utilized for investigating an ensemble of nano-sized magnets.[7–9] On the other hand, because of the poor sensitivity of conventional FMR spectroscopy, it is still challenging to perform an FMR experiment on an individual nano-sized magnetic material. As a result, the roles of many details in nano-sized magnetic materials, including sizes, shapes, and local structures on their magnetism and dynamics, have been largely unexplored.

In this paper, we discuss a method to perform FMR investigation on individual nano-sized ferromagnetic island structures using radio-frequency scanning tunneling spectroscopy (RF-STM). In the experiment of RF-STM, an RF electromagnetic wave is introduced into the tunneling gap through the probe tip of spin-polarized STM (SP-STM). When the magnetic resonance is induced on the spin situated just below the tip by the RF-modulated magnetic field, enhanced Larmor precession angle effectively reduces the spin component of the sample along the external magnetic-field direction, which can be detected through the measurement of the tunneling conductance using the spin-polarized tip.

Electron paramagnetic resonance (EPR) of single atoms[10,11] and molecules[12] have already been demonstrated using RF-STM. However, the mechanism of the single-atom/molecule resonance is not straightforward, since the amplitude of modulated RF magnetic field generated by RF electric field exerted between the tip and sample is zero just below the tip because of the rotational symmetry. The resonance is therefore believed to be caused by RF-modulated magnetic field induced by the presence of the magnetic tip; the modulated electric field vibrates the atomic/molecular position via the piezoelectric effect of the substrate, and then the local gradient of the effective exchange field due to the magnetized tip converts the vibration into the modulated magnetic field.[13] Despite the success of EPR on single atoms by RF-STM, utilizing the piezoelectronic coupling as a driving mechanism may not be applicable for larger magnetic structures such as magnetic nano islands. In fact, in the case of magnetic island structures, because of their finite lateral size, a significant amount of RF magnetic field is exerted on the sample away from the tip apex, enabling it to drive FMR directly. The detection of FMR has been indeed achieved on mm-size magnetic thin disks by using an RF probe tip.[14]

The primary goals of this paper are to calculate the amount of RF magnetic field below and around the tip apex in the configuration of RF-STM setup and to estimate the suitable condition for the FMR detection. For the nano-size magnetic sample, we consider a circular Co island with a thickness of two monolayers situated on a Cu(111) substrate, which exhibits perpendicular magnetic anisotropy.[15,16] The RF magnetic field around the tip apex was estimated from the calculation of near-field electromagnetic fields from the probe tip. Then, we solved the Landau–Lifshitz–Gilbert (LLG) equation,[17,18] which phenomenologically describes the precession of magnetization under magnetic fields, to obtain the amount of the reduced magnetization under the FMR and to simulate the FMR spectra of the individual nano-sized ferromagnetic island measured by RF-STM.

2. Model

The configuration of our calculated model is shown in Fig. 1. We simplify our sample, i.e. a nano-size ferromagnetic island

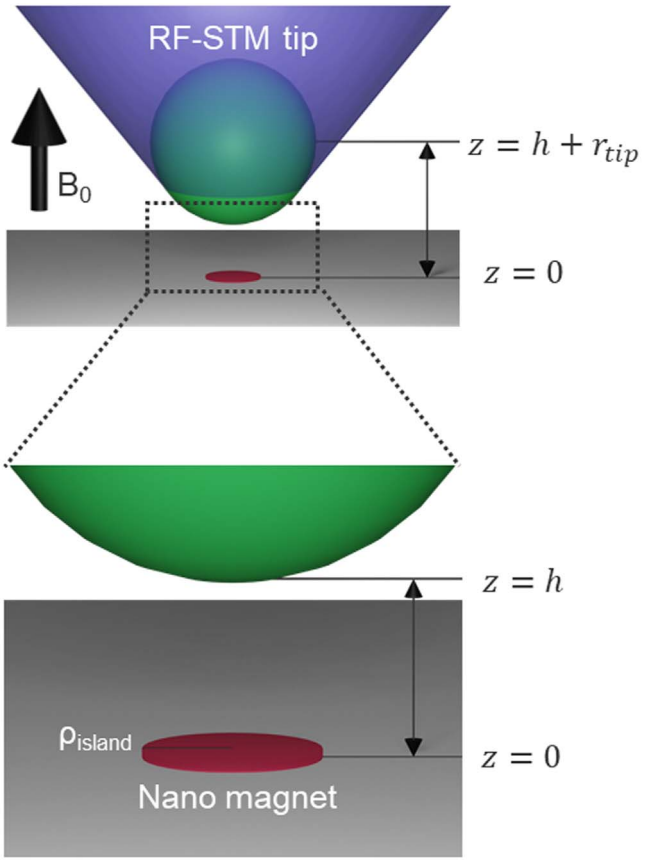

Fig. 1. (Color online) Configuration of the tip and sample in our calculation.

as a thin circular disk whose radius is ρ_{island} situated on an infinitely large conducting non-magnetic substrate. The probe tip is situated above the disk with the gap separation of h. We presume that the shape of the tip is symmetric rotationally with respect to the normal z-axis, and the curvature radius of the tip apex is given as r_{tip}. In the operation of RF-STM, RF-modulated voltage is added to dc bias voltage V_{DC} and connected to the probe tip using appropriate cables, and thus the tip apex is biased at $V_{DC} + V_{RF}e^{i\omega t}$, where V_{RF} and $f = 2\pi\omega$ are the amplitude and frequency of the applied RF voltage at the tip apex, respectively, with respect to the grounded sample.

3. Results

3.1. Electric and magnetic fields in the tunnel junction

When the tip-sample distance is much smaller than the curvature radius of the tip apex, and both are much shorter than the wavelength of the applied RF wave, the electromagnetic RF wave near the tip apex is reasonably assumed with the fields generated by an electric dipole $pe^{i\omega t}$ that points in the normal direction situated in vacuum at the position of the tip apex center, as shown in Fig. 2(a).[19–22] In a vacuum, the wave number is given as $k_2 = \omega/c$ using the speed of light c. On the other hand, in a substrate whose permittivity and conductivity are ε_1 and σ_1, respectively, the wave number is $k_1 = \omega\sqrt{\tilde{\varepsilon}_1/\varepsilon_0}/c$ using the complex permittivity $\tilde{\varepsilon}_1 = \varepsilon_1 - i\sigma_1/\omega$, where ε_0 is the permittivity of the vacuum. Here, we assume the permeability is uniform and the same as that of the vacuum μ_0 throughout the system, neglecting the presence of the magnetic sample and the magnetic tip apex.

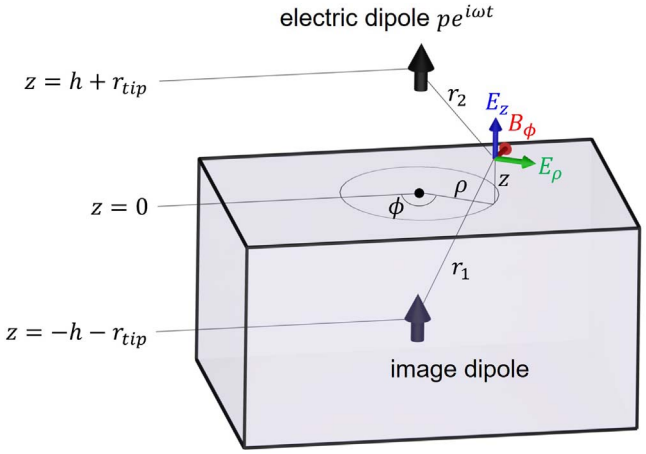

Fig. 2. (Color online) Schematic of electric image dipoles in our model. Blue and green arrows indicate z and radial components of generated electric fields at the position of (ρ, φ, z). The red arrow indicates generated magnetic field along the azimuthal direction. r_1 and r_2 indicate the distance from the image dipole and the electric dipole, respectively.

For the calculation of the electromagnetic fields around the tip-sample junction, the infinite conductive substrate can be replaced with an image dipole whose oscillatory frequency and polarity are the same as the original one. The amplitude of the image dipole is determined so that the boundary conditions for the electric field are satisfied at the substrate surface.

In this model, it is found that three components of the near-field electromagnetic wave are non-zero; z component of electric field E_z, radial component of electric field E_ρ, and azimuthal component of magnetic field B_ϕ in the cylindrical coordinates (Fig. 2). The other components are zero due to the rotational symmetry. According to previous papers that discuss the near-field scanning microwave microscopy,[19–22] the three components of the electromagnetic field generated by the two dipoles are described below:[23–25]

$$B_\phi(\rho, z) = -p\frac{\mu_0}{2\pi}\left[\frac{e^{ik_2r_1}}{2}\left(\frac{\rho}{r_1}\right)\left(\frac{ik_2}{r_1} - \frac{1}{r_1^2}\right) + \frac{e^{ik_2r_2}}{2}\left(\frac{\rho}{r_2}\right)\left(\frac{ik_2}{r_2} - \frac{1}{r_2^2}\right) - e^{ik_2r_2}\frac{k_2^3}{k_1}\left(\frac{\pi}{k_2r_2}\right)^{\frac{1}{2}}e^{-iP}\mathcal{F}(P)\right] \quad (1)$$

$$E_z(\rho, z) = p\frac{\omega\mu_0}{2\pi k_2}\left[\frac{e^{ik_2r_1}}{2}\left\{\frac{ik_2}{r_1} - \frac{1}{r_1^2} - \frac{i}{k_2r_1^3} - \left(\frac{z - d - r_{tip}}{r_1}\right)^2\left(\frac{ik_2}{r_1} - \frac{3}{r_1^2} - \frac{3i}{k_2r_1^3}\right)\right\} + \frac{e^{ik_2r_2}}{2}\left\{\frac{ik_2}{r_2} - \frac{1}{r_2^2} - \frac{i}{k_2r_2^3} - \left(\frac{z + d + r_{tip}}{r_2}\right)^2 \times \left(\frac{ik_2}{r_2} - \frac{3}{r_2^2} - \frac{3i}{k_2r_2^3}\right)\right\} - e^{ik_2r_2}\frac{k_2^3}{k_1}\left(\frac{\pi}{k_2r_2}\right)^{\frac{1}{2}}\left(\frac{\rho}{r_2}\right)e^{-iP}\mathcal{F}(P)\right] \quad (2)$$

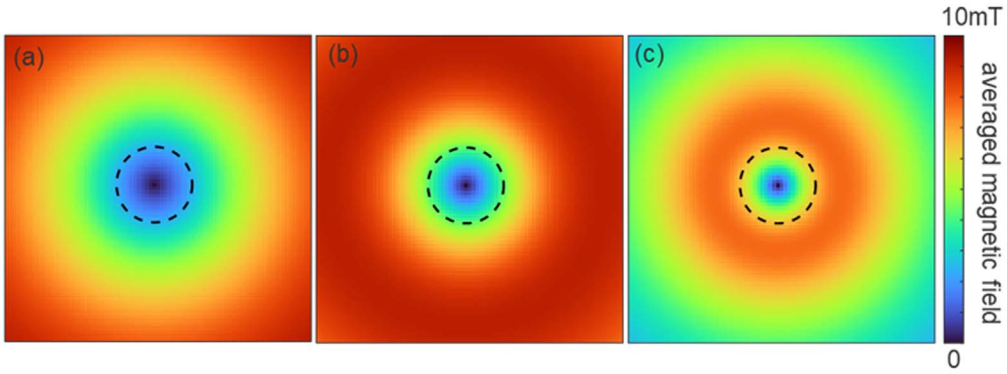

Fig. 3. (Color online) Calculated magnetic field averaged over a nano island (B_{RF}). Black dashed circle indicates the nano island whose radius is 10 nm. In this calculation we assume that the tip height h is 1nm, V_{RF} is 15 mV, and the tip radius r_{tip} is 100 nm, 50 nm, and 20 nm for (a)–(c), respectively. The calculated area is 80×80 nm^2.

$$E_\rho(\rho, z) = -p\frac{\omega\mu_0}{2\pi k_2}\left[\frac{e^{ik_2 r_1}}{2}\left(\frac{\rho}{r_1}\right)\left(\frac{z-d-r_{tip}}{r_1}\right)\right.$$
$$\times\left(\frac{ik_2}{r_1}-\frac{3}{r_1^2}-\frac{3i}{k_2 r_1^3}\right)+\frac{e^{ik_2 r_2}}{2}\left(\frac{\rho}{r_2}\right)\left(\frac{z+d+r_{tip}}{r_2}\right)$$
$$\times\left(\frac{ik_2}{r_2}-\frac{3}{r_2^2}-\frac{3i}{k_2 r_2^3}\right)-\frac{k_2}{k_1}e^{ik_2 r_2}$$
$$\left.\times\left\{\left(\frac{\rho}{r_2}\right)\left(\frac{ik_2}{r_2}-\frac{1}{r_2^2}\right)-\frac{k_2^3}{k_1}\left(\frac{\pi}{k_2 r_2}\right)^{\frac{1}{2}}e^{-iP}\mathcal{F}(P)\right\}\right], \quad (3)$$

where $P = \frac{k_2^3 r_2}{2k_1^2}\left[\frac{k_2 r_2 + k_1(z+d+r_{tip})}{k_2\rho}\right]^2$. r_1 and r_2 are the distances between the point (ρ, z) and the sites of the two dipoles, respectively, given as $r_1 = [\rho^2 + (z-h-r_{tip})^2]^{\frac{1}{2}}$ and $r_2 = [\rho^2 + (z+h+r_{tip})^2]^{\frac{1}{2}}$. $\mathcal{F}(P) = \int_P^\infty \frac{e^{it}}{(2\pi t)^{\frac{1}{2}}}dt = \frac{1}{2}(1+i) - C_2(P) - iS_2(P)$, where $C_2(P) + iS_2(P)$ is the Fresnel integral.

In our case, $|k_2/k_1| \sim \sqrt{\omega\varepsilon_0/\sigma_1} \sim 0$ is satisfied because the substrate is conductive and $\omega/2\pi$ is much smaller than its plasma frequency. In addition, the area we have interested in, where z is from 0 to h and ρ is in the order of the island size ($\sim$10 nm), is much smaller than the RF wavelength $\lambda_2 = 2\pi/k_2$ ($\lambda_2 \gg z$, h, ρ). $r_{tip} \gg h$, z is also satisfied as we assume $r_{tip} \sim 100$ nm and $h \sim 1$ nm. These inequalities simplify Eq. (1) at $z = 0$ and Eq. (2) for $\rho = 0$ in the following manner:

$$B_\phi(\rho, 0) \sim p\frac{\mu_0}{2\pi}\rho(\rho^2 + (r_{tip}+h)^2)^{-\frac{3}{2}} \quad (4)$$

$$E_z(0, z) \sim p\frac{\mu_0 c}{\pi}r_{tip}^{-2}. \quad (5)$$

In RF-STM we can experimentally measure the amplitude of the RF modulated voltage at the tip apex V_{RF} from the variation in tunneling spectra taken with RF and without RF,[10–12] as the RF-modulated bias voltage broadens tunneling spectra through the sinusoidal convolution. Since V_{RF} is equal to $E_z(0, z)h$ as $E_z(0, z)$ is constant with respect to z, we can estimate $B_\phi(\rho, 0)$ from V_{RF} by eliminating p from Eqs. (4) and (5) as follows:

$$B_\phi(\rho, 0) \sim \frac{V_{RF}}{2c}\frac{\rho r_{tip}^2}{h}(\rho^2 + (r_{tip}+h)^2)^{-\frac{3}{2}} \sim \frac{V_{RF}}{hc}\frac{\rho}{2r_{tip}}. \quad (6)$$

Equation (6) indicates that the azimuthal RF magnetic field, which induces FMR under the application of out-of-plane magnetic field,[14] is enhanced by using a sharp tip and by locating the tip close to the sample. The equation also indicates that the azimuthal component is zero just below the tip ($\rho = 0$) and increases proportionally to the distance from the tip apex (i.e. $B_\varnothing \sim \rho$).

We here assume that the magnetic island has a single domain processing uniformly in a concerted manner. This assumption is reasonable for nano-size islands whose magnetostatic energy is smaller than the domain wall formation energy, which is obviously satisfied for $\sim$10 nm radius islands. In the case of the single-domain magnets, the FMR-driving field is given effectively by the RF magnetic field averaged over the magnetic island. Since the RF magnetic field is a function of ρ, as shown in Eq. (6), the effective RF magnetic field depends on the position of the tip. Figure 3 shows a calculated two-dimensional map of the averaged magnetic field B_{RF} exerted on a circular disk as a function of the tip position. Here we assume the radius of nano-island is 10 nm, tip height $h = 1$ nm, RF-modulated bias voltage $V_{RF} = 15$ mV, and the radius of tip $r_{tip} = 100$ nm, 50 nm and 20 nm for Figs. 3(a)–3(c), respectively. At the center of the disk, the field is zero because of the rotational symmetry. With the distance from the center, the averaged in-plane magnetic field increases and is maximized around the disk edge. Since a significant in-plane RF-modulated magnetic field is exerted on the disk FMR can be driven under the external out-of-plane magnetic field, even when the tip is located outside of the disk.

The averaged magnetic field is polarized linearly in the direction perpendicular to the line connecting the tip position and the island center. The linearly-polarized RF field can be decomposed into two circularly-polarized magnetic fields with the amplitude of B_{RF} rotating in the clockwise and counter-clockwise directions with the RF frequency. Under the external magnetic field pointing upwards in the out-of-plane direction, the counter-clockwise field, which rotates in the same direction as Larmor precession, induces the

resonance. In the next section, we numerically solve the LLG equation using B_{RF} as an amplitude of the RF rotational magnetic field to elucidate the behavior of the resonance spectra.

3.2. FMR of nano-size magnetic disk

In RF-STM, where a spin-polarized tip is used as a probe, the amount of the spin-sensitive tunneling conductance is proportional to the component of sample magnetization parallel to the tip magnetization. At the resonance, the polar angle of the Larmor precession increases, resulting in the reduction in the effective magnetic moment along the precession axis. The resonance is, therefore, detected as a reduction in the spin-polarized tunneling conductance using a tip magnetized in the direction of the precession axis.

The FMR frequency and the precession angle under the RF magnetic field with a frequency of $\omega/2\pi$ can be obtained by solving the following LLG equation:

$$\frac{d\boldsymbol{m}}{dt} = -\gamma \boldsymbol{m} \times \boldsymbol{B} + \frac{\alpha}{m_0}\boldsymbol{m} \times \frac{d\boldsymbol{m}}{dt}, \tag{7}$$

where $\boldsymbol{m} = (m_x,\ m_y,\ m_z)$ is a magnetization vector of the sample, m_0 is the amplitude of $\boldsymbol{m}$, and α is a damping constant. γ is gyromagnetic ratio, equal to $g\mu_B/\hbar$, where g is g-factor and assumed 2.0 here, μ_B is Bohr magneton, and $\hbar$ is the Planck constant divided by 2π. $\boldsymbol{B}$ is a total magnetic field exerted on the sample that includes external static field $\boldsymbol{B}_0 = (0,\ 0,\ B_0)$, internal effective field induced by magnetic anisotropy $\boldsymbol{B}_a = (0,\ 0,\ B_a)$, and in-plane rotational RF magnetic field $\boldsymbol{B_{RF}}(t) = (B_{RF}\cos(\omega t),\ B_{RF}\sin(\omega t),\ 0)$, which was discussed in the previous session. In the case of the Co islands, which exhibits strong out-of-plane magneto-crystalline (or surface/interface) anisotropy over in-plane shape anisotropy, the anisotropic field is described as $B_a = 2\mu_0 K_a cos\theta/m_0$, where K_a is an anisotropic coefficient. Actually, in the case of single domain magnets like the Co nano islands $2\mu_0 K_a/m_0$ is equal to a coercivity B_c, which can be directly obtained with SP-STM through the measurement of the magnetic hysteresis.

Here we use the rotating frame $(\theta(t),\ \phi(t))$ around the z-axis with a frequency of $\omega/2\pi$ to describe the equation.[26–28] The magnetization $\boldsymbol{m} = (m_x,\ m_y,\ m_z)$ is written as:.

$$\begin{cases} m_x = m_0 sin\theta\cos(\omega t - \phi) \\ m_y = m_0 sin\theta\sin(\omega t - \phi). \\ m_z = m_0 cos\theta \end{cases} \tag{8}$$

By substituting $\boldsymbol{B} = \boldsymbol{B}_0 + \boldsymbol{B_a} + \boldsymbol{B_{RF}}$ and Eq. (8) into Eq. (7), simultaneous differential equations of $\theta(t)$ and $\phi(t)$ are obtained as follow:

$$\begin{cases} \alpha\dfrac{\mathrm{d}\theta}{\mathrm{d}t} + sin\theta\dfrac{d\phi}{dt} = \\ \gamma\left(\dfrac{\omega}{\gamma} - B_0 - B_c cos\theta\right)sin\theta + \gamma B_{RF} cos\theta cos\phi. \\ \dfrac{\mathrm{d}\theta}{\mathrm{d}t} - \alpha\, sin\theta\dfrac{d\phi}{dt} = \gamma\left(B_{RF} sin\phi - \dfrac{\alpha\omega}{\gamma}sin\theta\right) \end{cases} \tag{9}$$

In the steady state, $d\theta/dt = d\phi/dt = 0$, Substituting $\theta(t)=\theta_0$ and $\phi(t) = \phi_0$ into Eq. (9),

$$\begin{cases} \left(\dfrac{\alpha\omega}{\gamma}\, cot\phi_0 - B_c\right)cos\theta_0 = -\left(\dfrac{\omega}{\gamma} - B_0\right) \\ \left(\dfrac{\alpha\omega}{\gamma}\right)^2(\cot^2\phi_0 + 1)\sin^2\theta_0 = {B_{RF}}^2 \end{cases} \tag{10}$$

are obtained. By eliminating $\cot\phi_0$ from Eq. (10), we can obtain the equation of $\cos\theta_0$ as follows:[26,27]

$$1 - \cos^2\theta_0 = \frac{{B_{RF}}^2\cos^2\theta_0}{\delta^2 + \left(\frac{\alpha\omega}{\gamma}\right)^2\cos^2\theta_0}, \tag{11}$$

where $\delta = \frac{\omega}{\gamma} - (B_0 + B_c cos\theta_0)$. When the intensity of the RF field ($|B_{RF}|$) is small (i.e. $\theta_0 \sim 0$ and $\cos\theta_0 \sim 1$), the right side of Eq. (11), and θ_0 as well, are maximized at $\omega = \gamma(B_0 + B_c)$, which satisfies $\delta = 0$, and this corresponds to the resonance.

In order to investigate the behavior of $m_z \sim m_0 cos\theta_0$ beyond the restriction of $\theta_0 \sim 0$, we numerically calculated $cos\theta_0$ as a function of $\omega/2\pi$ by numerically solving the following biquadratic equation, which was expanded from Eq. (11):[28]

$$\begin{aligned} &-\left(B_c^2 + \left(\frac{\alpha\omega}{\gamma}\right)^2\right)\cos^4\theta_0 + 2B_c\left(\frac{\omega}{\gamma} - B_0\right)\cos^3\theta_0 \\ &+\left(B_c^2 + \left(\frac{\alpha\omega}{\gamma}\right)^2 - \left(\frac{\omega}{\gamma} - B_0\right)^2 - {B_{RF}}^2\right)\cos^2\theta_0 \\ &- 2B_c\left(\frac{\omega}{\gamma} - B_0\right)cos\theta + \left(\frac{\omega}{\gamma} - B_0\right)^2 = 0. \end{aligned} \tag{12}$$

As already described, B_{RF} can be adjusted thorough V_{RF} and B_a is given as a coercivity of the sample, which can be determined from a magnetic hysteresis measured by SP-STM. It has been known that the coercivity of Co nano-sized islands is dependent on the island size; e.g. 1.25 T for an island whose area is 130 nm^2 and 1.625 T for 250 nm^2 island.[16] In our calculation, we use these two values for B_c. B_0 is an experimental parameter. α and m_0 are unknown parameters; they can be obtained from the fitting of experimentally obtained FMR spectra.

Figures 4(a)–4(b) shows the calculated spectra of $cos\theta_0$ as a function of the RF frequency. In the calculation, the tip position is set at 5 nm from the center of the island. The other parameters are listed in Table I. Note that the amount of $cos\theta_0$ is the z component ratio of the magnetization, and therefore, proportional to the amount of the spin-polarized tunneling conductance with a tip magnetized in the z direction. We can see a dip in the spectra due to the resonance. For small RF amplitude V_{RF} (30 mV), the dip is small and its shape is symmetric. The dip frequency is almost equal to that estimated from $\omega = \gamma(B_0 + B_c)$ as θ is negligibly small. Since the resonance frequency is proportional to $B_0 + B_c$, an island with large coercivity shows a dip at higher frequency. With increasing in V_{RF}, θ increases, and the spectra basically follow the line of $\omega = \gamma(B_0 + B_c cos\theta)$. Thus, the dip shifts to lower frequency, resulting in an asymmetric shape. For large V_{RF} (60 mV), the spectra exhibit a hysteresis known as a

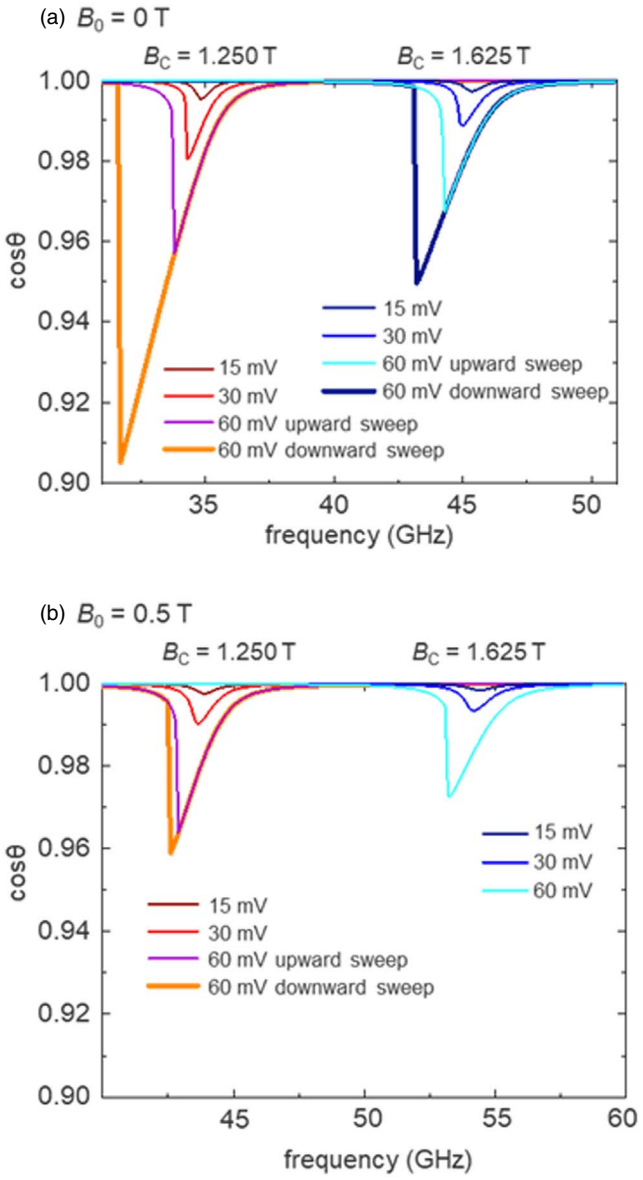

Fig. 4. (Color online) Calculated spectra of $\cos\theta_0$ as a function of the RF frequency under (a) $B_0 = 0$ T and (b) $B_0 = 0.5$ T. In this calculation, we assume that the coercivity $B_c = 1.25$ T (left side in each graph) $B_c = 1.625$ T (right side) and $V_{RF} = 15$ mV, 30 mV and 60 mV. Other parameters are listed on Table I.

Table I. Parameters for the calculation shown in Fig. 4.

Applied field B_0	0, 0.5 T
Coercivity B_c	1.250, 1.625 T
Damping constant α	0.01
Modulation amplitude V_{RF}	15, 30, 60 mV
Curvature radius r_{tip}	100 nm
Radius of island ρ_{island}	10 nm
Tip-sample height h	1 nm

foldover effect.[27–31] The downward sweep takes a deeper trace than the upward sweep. Note that the asymmetric shape and the folding effect are caused by the effective magnetic field due to the out-of-plane magnetic anisotropy. Since the damping term $\alpha\omega/\gamma$ [see Eq. (11)] is proportional to the frequency, dips at lower frequency are deeper than higher frequency dips.

The frequency of RF required for the detection of these FMR spectra is rather high (>28 GHz). This is simply due to large coercivity B_c of the Co islands, as the resonance frequency is basically given by $\omega = \gamma(B_0 + B_c)$. In order to reduce the frequency down to the range experimentally feasible, the coercivity should be reduced. It is recently reported that alloying with Fe significantly reduces the coercivity of the Co islands.[32,33] Strong electric field, which can be achieved by situating the tip closer to the sample, may also reduce the coercivity by field-induced reduction in perpendicular magnetic anisotropy.[34]

4. Conclusion

In this paper, we first numerically calculated the amount of in-plane magnetic field exerted on a nano-sized circular disk, which drives FMR when the disk is out-of-plane magnetized, in the configuration of RF-STM, where RF electromagnetic waves are introduced into the tunneling gap through the STM tip. We found that a sharp tip and small tip-sample gap distance enhance the amount of the RF magnetic field. It is also found that the field is maximized when the tip is located at the edge of the island. Then using the amount of the RF-modulated magnetic field, we numerically simulated the FMR spectra expected on Co nano islands formed on Cu(111) substrate. The spectra demonstrate that the resonance frequency strongly depends on the coercivity of the island. When the amount of the RF magnetic field is small the spectrum is symmetric, but with the increment in the RF field, the spectrum becomes asymmetric and further increase makes the spectrum exhibit a hysteresis due to the folding effect. Our results reveal the conditions to induce and detect FMR on nano-sized magnetic structures using RF-STM.

Acknowledgments

This work is partially supported by Grants-in-Aid for Scientific Research from the Japan Society for the Promotion of Science (Grants No. JP16H02109, No. JP18K19013, No. JP19H00859, and No. JP20K15166). ST acknowledges support from the US National Science Foundation (DMR-1508661, CHE-1611134, and CHE-2004252 with partial co-funding from the Quantum Information Science program in the Division of Physics).

ORCID iDs

Susumu Takahashi https://orcid.org/0000-0002-1302-2845
Yukio Hasegawa https://orcid.org/0000-0002-6674-4745

1) M. Vogel, A. V. Chumak, E. H. Waller, T. Langner, V. I. Vasyuchka, B. Hillebrands, and G. von Freymann, Nat. Phys. **11**, 487 (2015).
2) A. V. Chumak, V. I. Vasyuchka, A. A. Serga, and B. Hillebrands, Nat. Phys. **11**, 453 (2015).
3) A. Haldar, D. Kumar, and A. O. Adeyeye, Nat. Nanotechnol. **11**, 437 (2016).
4) E. Saitoh, M. Ueda, H. Miyajima, and G. Tatara, Appl. Phys. Lett. **88**, 182509 (2006).
5) K. Ando, Y. Kajiwara, S. Takahashi, S. Maekawa, K. Takemoto, M. Takatsu, and E. Saitoh, Phys. Rev. B **78**, 014413 (2008).
6) K. Ando et al., J. Appl. Phys. **109**, 103913 (2011).
7) M. R. Diehl, J.-Y. Yu, J. R. Heath, G. A. Held, H. Doyle, S. Sun, and C. B. Murray, J. Phys. Chem. B **105**, 7913 (2001).
8) L. F. Gamarra, W. M. Pontuschka, J. B. Mamani, D. R. Cornejo, T. R. Oliveira, E. D. Vieira, A. J. Costa-Filho, and E. A. JR, J. Phys.: Condens. Matter **21**, 115104 (2009).
9) I. Nekrashevich and D. Litvinov, AIP Adv. **8**, 085002 (2018).

10) S. Baumann, W. Paul, T. Choi, C. P. Lutz, A. Ardavan, and A. J. Heinrich, Science **350**, 417 (2015).
11) P. Willke, Y. Bae, K. Yang, J. L. Lado, A. Ferrón, T. Choi, A. Ardavan, J. Fernández-Rossier, A. J. Heinrich, and C. P. Lutz, Science **362**, 336 (2018).
12) S. Müllegger, S. Tebi, A. K. Das, W. Schöfberger, F. Faschinger, and R. Koch, Phys. Rev. Lett. **113**, 133001 (2014).
13) J. L. Lado, A. Ferrón, and J. Fernández-Rossier, Phys. Rev. B **96**, 205420 (2017).
14) T. An, N. Ohnishi, T. Eguchi, Y. Hasegawa, and P. Kabos, IEEE Mag. Lett. **1**, 3500104 (2010).
15) G. Rodary, S. Wedekind, D. Sander, and J. Kirschner, Jpn. J. Appl. Phys. **47**, 9013 (2008).
16) S. Ouazi, S. Wedekind, G. Rodary, H. Oka, D. Sander, and J. Kirschner, Phys. Rev. Lett. **108**, 107206 (2012).
17) L. Landau and E. Lifshitz, *Perspectives in Theoretical Physics* (Elsevier, Amsterdam, 1992), p. 51.
18) T. L. Gilbert, Phys. Rev. **100**, 1243 (1955).
19) A. Imtiaz and S. M. Anlage, J. Appl. Phys. **100**, 044304 (2006).
20) D. I. Mircea and T. W. Clinton, Appl. Phys. Lett. **90**, 142504 (2007).
21) A. N. Reznik and V. V. Talanov, Rev. Sci. Instrum. **79**, 113708 (2008).
22) A. Imtiaz, T. Baldwin, H. T. Nembach, T. M. Wallis, and P. Kabos, Appl. Phys. Lett. **90**, 243105 (2007).
23) R. W. P. King, J. Appl. Phys. **53**, 8476 (1982).
24) R. W. P. King, Radio Sci. **25**, 149 (1990).
25) R. W. P. King and S. S. Sandler, Radio Sci. **29**, 97 (1994).
26) G. Bertotti, C. Serpico, and I. D. Mayergoyz, Phys. Rev. Lett. **86**, 724 (2001).
27) W. Scholz and S. Batra, J. Appl. Phys. **103**, 07F539 (2008).
28) M. d'Aquino, A. Quercia, V. Scalera, S. Perna, G. Bertotti, I. D. Mayergoyz, and C. Serpico, IEEE Trans. Magn. **53**, 4301005 (2017).
29) P. W. Anderson and H. Suhl, Phys. Rev. **100**, 1788 (1955).
30) Y. S. Gui, A. Wirthmann, and C.-M. Hu, Phys. Rev. B **80**, 184422 (2009).
31) Y. S. Gui, A. Wirthmann, N. Mecking, and C.-M. Hu, Phys. Rev. B **80**, 060402(R) (2009).
32) H.-H. Yang, C.-H. Hsu, W.-C. Lin, and Y. Hasegawa, Phys. Rev. B **104**, 035422 (2021).
33) H.-H. Yang, C.-C. Hsu, K. Asakawa, W.-C. Lin, and Y. Hasegawa, Nanoscale **13**, 16719 (2021).
34) S. Miwa et al., J. Phys. D **52**, 063001 (2019).